

Two-domains bulklike Fermi surface of Ag films deposited onto Si(111)-(7x7)

J.F. Sánchez-Royo

*LURE, Centre Universitaire Paris-Sud, Bat. 209 D, B.P. 34, 91898 Orsay Cedex, France
and Dpt. Física Aplicada, ICMUV, Univ. de Valencia, c/Dr. Moliner 50, 46100 Burjassot, Valencia, Spain*

J. Avila

*LURE, Centre Universitaire Paris-Sud, Bat. 209 D, B.P. 34, 91898 Orsay Cedex, France
and Instituto de Ciencia de Materiales de Madrid, CSIC, Cantoblanco, 28049 Madrid, Spain*

V. Pérez-Dieste

LURE, Centre Universitaire Paris-Sud, Bat. 209 D, B.P. 34, 91898 Orsay Cedex, France

M. De Seta

Dipartimento di Fisica, Università di Roma III, I-00146 Roma, Italy

M.C. Asensio*

*LURE, Centre Universitaire Paris-Sud, Bat. 209 D, B.P. 34, 91898 Orsay Cedex, France
and Instituto de Ciencia de Materiales de Madrid, CSIC, Cantoblanco, 28049 Madrid, Spain
(November 1, 2018)*

Thick metallic silver films have been deposited onto Si(111)-(7x7) substrates at room temperature. Their electronic properties have been studied by using angle resolved photoelectron spectroscopy (ARPES). In addition to the electronic band dispersion along the high-symmetry directions, the Fermi surface topology of the grown films has been investigated. Using ARPES, the spectral weight distribution at the Fermi level throughout large portions of the reciprocal space has been determined at particular perpendicular electron-momentum values. Systematically, the contours of the Fermi surface of these films reflected a sixfold symmetry instead of the threefold symmetry of Ag single crystal. This loss of symmetry has been attributed to the fact that these films appear to be composed by two sets of domains rotated 60° from each other. Extra, photoemission features at the Fermi level were also detected, which have been attributed to the presence of surface states and *sp*-quantum states. The dimensionality of the Fermi surface of these films has been analyzed studying the dependence of the Fermi surface contours with the incident photon energy. The behavior of these contours measured at particular points along the Ag Γ L high-symmetry direction puts forward the three-dimensional character of the electronic structure of the films investigated.

PACS numbers: 68.35.-p, 71.18.+y, 73.20.-r, 79.60.-i

I. INTRODUCTION

Silicon (Si) surfaces have been extensively investigated over the last decades and, consequently, a huge knowledge exists on their structural and electronic properties.^{1,2} In spite of it, some questions still remain open, particularly those related with their electronic properties and surface dynamics.^{3,4} Both their fundamental and technological importance stand for the large interest on the Si surfaces. Among semiconductor materials, the Si(111) system is one of the most interesting due to the complexity of its surface structure. The existence of unoccupied dangling bonds at the bare semiconductor surface leads to a strong chemical activity on it. In consequence, the addition of foreign elements can drastically modify its atomic structure and electronic properties. In this context, a large interest has been aroused around the reconstructed surfaces derived by the addition of metallic adatoms, in particular on first stage of silver (Ag) adsorption, and also on thick metallic films deposited onto pure

Si(111) surface reconstructions.²

By far, the most commonly studied Ag/Si(111) systems are those of Ag films deposited onto the Si(111)-(7x7) and the Ag-derived Si(111)- $(\sqrt{3} \times \sqrt{3})R30^\circ$ surface reconstruction. The case of the (7x7) surface reconstruction is specially attractive since its unit cell shows a reduction in the number of dangling bonds, compared to the ideal (1x1) surface termination, and it shows two opposite stacking sequences, one of them having stacking fault. The peculiar structure of the (7x7) Si termination determines the dynamics of adatoms at the surface. Scanning tunneling microscope measurements carried out in submonolayer Ag films deposited at room temperature onto Si(111)7x7 substrates showed that Ag preferentially condenses on the faulted halves of the (7x7) reconstruction.^{5,6} In this situation, films tend to form clusters of few tens of Ag atoms, already at a coverage of 0.25 monolayers (MLs), with an interatomic distant close to that of Ag single crystal.^{7,8} As the film thickness increases, the covered halves of the (7x7) unit cell

tend to join each other,⁷ and further deposition tends to cover the whole surface. After few Ag MLs, multilayered three-dimensional (3D) Ag islands start to nucleate on the clusters.^{8,9} Impact-collision ion-scattering spectroscopy measurements revealed that Ag(111) films of several MLs deposited onto Si(111)-(7x7) at room temperature consist of domains of Ag(111) crystals rotated 60° around the surface normal, in approximately the twin relation,¹⁰ with their $\langle\bar{1}10\rangle$ directions parallel to those of the substrate.^{11,12}

In this context, the electronic properties of the surface develop from those of the (7x7) surface to those determined by metallic bulklike Ag films. Particularly important are the states closest to the Fermi level (E_F). They are responsible for electron transport properties as they define the Fermi surface (FS) and a potential Mott transition at low temperatures. The (7x7) surface exhibits two nearly dispersionless surface states centered at binding energies of 0.2 and 0.9 eV below the E_F ,^{13–18} which have been assigned to the dangling-bond and rest-atom states, respectively. In addition, a back-bond state has been also observed at 1.8 eV below the E_F near the boundary of the (1x1) surface Brillouin zone (BZ).^{19,20} These states can be clearly separated from each other and from the bulk semiconductor electronic states. The possible metallic behavior of this surface comes through the fact that the surface E_F is strongly pinned due to the high density of surface states near or at the E_F .²¹ In order to elucidate the degree of localization of the characteristic surface states of the (7x7) surface reconstruction, different techniques have been applied, such as conductivity,²² nuclear-spin resonance,²³ and angle-resolved photoemission measurements.³ Nevertheless, it is not well established yet the metallic behavior of the surface state bands close to the E_F . Also, a possible existence of a small gap at the surface has been discussed.³

After deposition of Ag adatoms, the electronic properties of the surface are strongly modified, since they are determined by the atomic deposition, diffusion at the interface, and nucleation of the incipient films, which conclude as bulklike thick Ag films. At first stage of Ag deposition, valence-band spectra photoemission measurements revealed a quick suppression of the dangling-bond state of the (7x7) surface with a Ag coverage of 0.2 MLs,²⁴ clearly converting the surface into semiconducting. This result is consistent with scanning tunneling spectroscopy measurements,⁵ which revealed a semiconducting behavior of the Ag-covered areas of the surface in comparison to the uncovered ones. Nevertheless, the increase of resistivity appears to be shorter than that expected for a suppression of the strongly localized (7x7) surface-state bands.^{25–27} As the Ag coverage increases, the surface turns to be metallic, due to the bulklike behavior of thick Ag films, and its conductivity appears to be well described by a Drude model, with a linear coefficient close to the characteristic bulk value at temperatures higher than 40 K.^{28,29} Nevertheless, this behavior has not been connected yet with the electronic properties of the films

at the E_F , that is, with the topology of the FS.

In this work, we study the electronic properties and, particularly, the FS of thick Ag films deposited onto Si(111)-(7x7) substrates at room temperature, in order to establish the limiting electronic conditions of the work-frame in which the conductivity and transport properties of Ag/Si(111)-(7x7) interfaces can be considered as determined by metallic Ag bulklike films. For this purpose, angle-resolved photoelectron spectroscopy (ARPES) appears to be one of the most powerful and direct tools to probe the electronic structure of solids. By directly measuring single-particle excitation spectra (also called spectral weight) as a function of momentum and energy, it can be determined the most basic quantities of condensed matter physics, e.g. the band structure, dimensionality of electronic states, the symmetry and a quantitative analysis of the FS, electronic gap opening, nesting vector, and so forth.

This paper is organized as follows. Section II summarizes the experimental details. The results obtained by ARPES are showed and discussed in Sect. III. In this section it is described the experimental procedure to obtain by ARPES the spectral function defining the FS of metallic/semiconductor interfaces. Next, it is illustrated and discussed the spectral weight at the E_F measured in the studied Ag films, in order to extract and analyze their FS. We finish this section with the analysis of the *quasi*-two-dimensional (*quasi*-2D) or 3D character of the investigated interfaces by means of their experimentally determined FS. The last section (IV) is devoted to summarize the ARPES results and focus in the conclusions of this work.

II. EXPERIMENTAL

The experiments were performed at LURE (Orsay, France) using the Spanish-French (PES2) experimental station of the Super-Aco storage ring, described elsewhere.³⁰ The measurements were carried out in a purpose-built ultra-high vacuum system, with a base pressure of 5×10^{-11} mbar, equipped with an angle resolving 50 mm hemispherical VSW analyzer coupled on a goniometer inside the chamber. The manipulator was mounted in a two-axes goniometer which allows rotation of the sample in the whole 360° azimuthal angle and in the 180° polar emission angle relative to surface normal (Θ_{off}), with an overall angular resolution of 0.5°. Photoelectrons were excited with p-polarized synchrotron radiation in the 18-150 eV energy range. In our experiments, the incident angle of the light was fixed at 45°. In these conditions, changes of polarization effects on initial states are neglected.

With this set-up, the procedure to determine the FS using ARPES is direct. For a given experiment, the photon energy ($h\nu$) was fixed and the intensity at the E_F was recorded, along a series of azimuthal scans, for each step

of the crystal rotation about its surface normal. This procedure was repeated at different polar angle positions of the analyzer, which allow us to scan a sheet of the BZ for each excitation energy. In order to measure the FS contours at different perpendicular wave vectors, the above procedure was carried out at different photon energies. In our measurements, typical polar intervals were 1.5° and the azimuthal angle range was fixed at 180° . Depending on statistics and optimal signal-to-noise ratio, a typical measuring time of 4 to 6 hours was required to record a FS throughout the whole BZ.

The p-doped Si(111) single crystal substrate (with a nominal resistivity of $0.02 \Omega\text{cm}$) was heated up to 650°C , in order to degas the wafer, during several hours by resistive heating and then repeatedly flashed at 1100°C during no more than 15 seconds. Structural order quality was checked out by low-energy electron diffraction measurements (LEED), which showed sharp spots corresponding to a distinctive Si(111)-(7x7) surface reconstruction. In addition to this, no surface impurities were detected by synchrotron radiation photoemission measurements. The Si(111)-(7x7) substrate was oriented by azimuthal and polar photoelectron diffraction (PhD) scans recording the Si 2p peak intensity.³¹ Ag was evaporated onto the surface at room temperature. The evaporation rate used (of 0.06 MLs/min) was determined by using a quartz microbalance. In these conditions thick Ag films, of approximately 10 MLs in thickness, were deposited. In order to improve their structural quality, the samples were systematically annealed to 240°C for 30 min. LEED spectra measured after growth revealed a clear Ag (1x1) hexagonal pattern.

III. RESULTS AND DISCUSSION

A. Determination of the Fermi Surface by using ARPES

This section is devoted to describe the experimental determination of the FS of thick Ag films epitaxially grown on Si (111)-(7x7) substrates by using ARPES. In order to unify the nomenclature to be used describing our measurements, we show in Figure 1 the bulk BZ of Ag single crystal together with the characteristic high-symmetry directions associated to it. The Ag BZ is the typical one for a fcc material. The (111)-face is hexagonal alternatively surrounded by hexagonal and square faces. The schematic representation of Fig. 1 puts forward the threefold symmetry of the BZ with respect to the [111] direction. The surface BZ along the [111] direction is hexagonal and its $\bar{\Gamma}$ -point is the projection of the Γ L high-symmetry direction of the bulk BZ. The projections of the L and X points of the BZ lie on the \bar{M} and \bar{M}' points of the surface BZ, respectively. The high-symmetry directions of the (111) surface BZ are also indicated.

Figure 2 shows the well-known theoretical FS of bulk Ag single crystal oriented as a function of the high-symmetry directions.³² The Ag FS is mainly defined by *sp*-states lying at the E_F . As predicted by the nearly free-electron model, the FS is almost spherical with a volume half of the BZ volume. Nevertheless, the spherical shape of the FS is distorted. This is a consequence of the hybridization of the *sp*-band with the filled *d* band also close to the E_F , which makes individual spheres touch each other at the BZ boundary close to the $\langle 111 \rangle$ directions. Typical *necks* and *bones* are then clearly identified around the L and X points, respectively.

The FS determined by using ARPES can be easily connected with the band structure diagrams. Figure 3 shows our results of calculations of the band structure of fcc Ag single crystal using a tight-binding hamiltonian. The theoretical simulations allow us to show clearly the direct relation between the 2D cut of the 3D FS and the traditional band structure diagrams. Figures 3(a) and 3(b) show the band structure diagram of Ag single crystal along the $[1\bar{1}0]$ and $[11\bar{2}]-[\bar{1}\bar{1}2]$ high-symmetry directions, respectively.³³ In order to calculate which perpendicular electron-momentum (k_\perp) value was probed when $h\nu=32 \text{ eV}$ was used, we have assumed free-electron final states as well as a work function (Φ) value of $\Phi=4.5 \text{ eV}$. With regards to the inner potential (V_o) we have considered it as a parameter. As a consequence of the no-conservation of k_\perp during the photoemission process, we find the right value of the V_o by fitting the theoretical results to the experimental spectral weight at the E_F . In this way, we have obtained a value of $V_o=-11.5 \text{ eV}$, which is quite close to that early concluded by Wu *et al.* ($V_o \sim -10 \text{ eV}$).³⁴ The Ag band structure diagrams of Figs. 3(a) and 3(b) show states lying at the E_F at different parallel momentum (k_\parallel) values along the indicated high-symmetry directions. In essence, the experimental determination of a 2D cut of the FS by using ARPES requires scanning of the photoemission signal from states at the E_F throughout large portions of the reciprocal space. As an example of the theoretical FS cut in the k_\parallel -plane to be measured by using ARPES, we show in Fig. 3(c) the 2D FS cut of Ag single crystal when a photon energy of 32 eV has been used to perturb the ordered metallic layer.³³

Photoemission process involves energy and crystal momentum conservation. In the frame of the three-step model of the photoexcitation mechanism in ARPES, momentum of the electrons inside a bulk material can be determined. In this case, both momentum components, k_\parallel and k_\perp , of photoexcited electrons from states at the E_F can be expressed as³⁵

$$k_\parallel = \sqrt{\frac{2m}{\hbar^2}} \sqrt{h\nu - \Phi} \sin(\Theta_{off}) \quad (1a)$$

and

$$k_\perp = \sqrt{\frac{2m}{\hbar^2}} \sqrt{(h\nu - \Phi) \cos^2(\Theta_{off}) - V_o}, \quad (1b)$$

where m is the free-electron mass and \hbar is the reduced Planck constant. These equations directly imply that, using a constant $h\nu$, all the initial states with a parabolic shell (k_{\parallel}, k_{\perp}) of the BZ are probed. Figure 4 shows a transversal cut of the bulk Ag BZ in the extended zone scheme. This schematic view corresponds to the cut of the Ag BZ by the plane defined by the $[111]$ and $[\bar{2}11]$ high-symmetry directions. The most important points are also indicated. The intersection of the Ag FS of contiguous BZs with that plane is also shown, which forms the so-called dog-bones contours. In the figure, they are also indicated successive parabolic shells throughout the bulklike Ag FS obtained by using Eqs. (1) for $h\nu=32$, 55, and 96 eV. They have been calculated for Θ_{off} values ranging between 0° and 55° , which correspond to our typical experimental conditions. The intersection between the Ag FS and these parabolic shells defines 2D FS contours, which pass close to the middle between the Γ and L points for $h\nu=32$ eV, near the L point for $h\nu=55$ eV, and near to the Γ point for $h\nu=96$ eV.

As a summary, we can emphasize that the ability of the ARPES technique to determine *in situ* FS contours and band dispersion of metallic systems, can be envisaged as a very valuable methodology to experimentally characterize the electronic properties of novel materials. Nevertheless, it should be pointed out that extracting the FS contour from the experimental spectral weight at the E_F can not be considered as an easy task, mostly in low-dimensional materials,³⁶ where strong matrix element variations can occur. In spite of this and, in contrast to the Haas-van Alphen method, ARPES technique can be used to study a wide variety of low-dimensional metallic materials like alloys and highly-correlated electron systems.^{37,38} Additionally, the contours of the FS using ARPES can be measured throughout all the BZ directions, which allows us to focus a detailed study of the topology of the FS at particular portions of the reciprocal space.

B. The Fermi Surface of 10 ML Ag(111) films grown on Si(111)-(7x7) substrates

Figure 5 shows the experimental 2D FS cut measured in 10 ML-thick Ag films using light of $h\nu=32$ eV. The upper half part of the image corresponds to the measured data. The lower part is the result of the symmetrization of the measured data with respect to x-axis. Photoelectron angular distribution measurements are indicated by taking x-axis as the $[\bar{1}10]$ direction of the crystal. The identification of the high symmetry directions of the surface by LEED measurements before and after the Ag deposition allows us to confirm that the Ag(111) films onto Si(111)-(7x7) grow epitaxially with the Ag overlayer $\langle\bar{1}10\rangle$ high-symmetry directions parallel to those of the Si substrate, as it has been previously reported.^{11,12} The image has been scaled in such a way that it is linear in photoemission intensity and in k_{\parallel} . Nevertheless, it

should be said that the central part of the image ($k_{\parallel}<0.4$ \AA^{-1}) was background-enhanced by a constant factor of 2, in order to appear visible in the image. The photoemission intensity is maximum for the brightest feature and minimum for the darkest one. In this image, well-defined features are labelled, indicating the momentum distribution of initial states lying at the E_F as a function of k_{\parallel} and k_{\perp} .

Figure 6(a) shows the theoretical 2D cut of the ideal Ag single crystal FS at a particular k_{\perp} value defined by a parabolic shell determined by a photon energy of $h\nu=32$ eV (see Eqs. (1)).³³ This 2D contour reflects directly the typical threefold symmetry of a fcc material, which can be described as a distorted ringlike feature (FS1 feature) with a maximum value of the Fermi momentum (k_F) of $k_F=1.29$ \AA^{-1} along the $\langle\bar{1}12\rangle$ directions, a value of $k_F=1.17$ \AA^{-1} along the $\langle\bar{2}11\rangle$ directions, and a minimum value of $k_F=1.13$ \AA^{-1} along the $\langle\bar{1}10\rangle$ directions. According to the BZ extended zone scheme, additional contributions to the FS from neighboring BZs are also expected in the $\langle\bar{2}11\rangle$ direction (FS2 features) as well as along the $\langle\bar{1}12\rangle$ direction (FS2' features).

The experimental photoelectron spectral weight image at the E_F (Fig. 5) exhibits most of the characteristic features predicted for a FS of a bulklike Ag single crystal (Fig. 6(a)). Nevertheless, the experimental FS contour shows a sixfold rather than the typical threefold symmetry of the FS contour of bulklike fcc Ag single crystal. This clear result is a consequence of the two-domain character of the Ag films grown onto Si substrates. Forward scattering PhD has demonstrated that the metallic films grow epitaxially oriented with respect to the substrate and that the overlayer consists of two domains of fcc Ag lattices rotated 60° from each other.³⁹ As PhD is a technique that probes and averages large portions of the interface, we will have two independent contributions to the photoelectron signal from the two coexisting metallic domains. Therefore, the photoelectrons with k_{\parallel} corresponding to $[\bar{2}11]$ and $[\bar{1}12]$ directions of two inequivalent domains will overlap in the recorded photoemission signal. Fig. 6(b) shows the theoretical Ag FS cut calculated for two domains rotated 60° for $h\nu=32$ eV, which is in excellent agreement with the experimental data shown in Fig. 5.

In order to carry out a more quantitative analysis of the spectral weight images as obtained by ARPES we have followed the procedure proposed by Straub *et al.*⁴⁰ The experimental method used to obtain an image as that shown in Fig. 5 involves selecting an energy window around the E_F . The intensity in this window is represented as a function of k_{\parallel} ($w(k_{\parallel})$ function). In that work, the authors have analyzed how the width of the energy window, usually limited by the experimental resolution, affects the measured FS images. A method was proposed to extract from the FS images the correct values of k_F as well as the different k_{\parallel} values of the FS cuts, which can be affected by the experimental resolu-

tion. It involves the calculation of the gradient of the FS images ($|\nabla_{k_{\parallel}} w(k_{\parallel})|$). This procedure produces two maxima out of each maximum of the spectral weight at the E_F (Fig. 5). It was found that, out of the two maxima of the gradient, the one on the unoccupied side of the band crossing the E_F accurately reflects the k_{\parallel} values of the FS cuts.

Analyzing the measured spectral weight image by this method, we have obtained the gradient of the image showed in Fig. 5. This is displayed in Figure 7, together with the two-domains Ag FS cut calculated for $h\nu=32$ eV (Fig 6(b)). The FS1, FS2, and FS2' features labelled in Fig. 7 are fairly reproduced by the Ag FS cut calculated. Nevertheless, the FS2 feature obtained by calculations is shifted by $\Delta\text{FS2}=0.3 \text{ \AA}^{-1}$ respect to the experimental data. This considerable shift of the contours of the FS mostly appears in neighboring BZs rather than in the first BZ. This disagreement between the calculated and experimental Ag FS cut could be attributed to non-parabolic final states transitions. In fact, LEED measurements together with constant-final-states photoemission measurements in the related fcc Cu compound have demonstrated the influence of unoccupied band structure in the accuracy of valence band dispersion determination.⁴¹ Recently, the combined use of LEED and ARPES has revealed that the unoccupied band dispersion shows a significant deviation from the free-electron-like behavior. A similar situation could be expected for the band structure of Ag. The fact that the FS cut calculated for $h\nu=32$ eV shows a large misfit only in neighbors BZs can also be attributed to a stronger than k_{\perp} -dependency of the Ag FS as it has been considered in this work (see Fig. 4).

Figure 8 shows the profile of both the spectral weight at the E_F measured with $h\nu=32$ eV and its gradient along the $\langle\bar{1}10\rangle$ directions (Fig. 8(a)) and along the $\langle\bar{1}\bar{1}2\rangle$ and $\langle\bar{2}11\rangle$ overlapped directions (Fig. 8(b)). Following the Straub *et al.* procedure,⁴⁰ we have obtained average values of $k_F=1.21 \pm 0.06 \text{ \AA}^{-1}$ along the $\langle\bar{1}10\rangle$ directions and $k_F=1.34 \pm 0.06 \text{ \AA}^{-1}$ along the $\langle\bar{1}\bar{1}2\rangle$ and $\langle\bar{2}11\rangle$ directions. These experimental values are in concordance with those obtained by tight-binding calculations showed in Fig. 6.

Whereas the 2D Ag FS cut for $h\nu=32$ eV in contiguous BZs is correctly reproduced by the results of tight-binding, there are some particular experimental features that are not theoretically predicted. Figure 7 illustrates the *s* and *h* features. The *s* feature appears as a rather diffuse ringlike feature at $\sim 0.26 \text{ \AA}^{-1}$ with an intense spot at the center of the image of 0.10 \AA^{-1} in radius. The *h* feature is a diffuse fluted contour at $k_{\parallel}\sim 0.7 \text{ \AA}^{-1}$ that appears under the FS cut in the first BZ in the $\langle\bar{1}\bar{1}2\rangle$ and $\langle\bar{2}11\rangle$ directions and seems to connect points of the FS cut in the $\langle\bar{1}10\rangle$ directions.

In order to analyze the behavior of these unexpected features, we have measured the band dispersion of the Ag films along the $[\bar{1}10]$ direction and along the $[\bar{1}\bar{1}2]$ and $[\bar{2}11]$ coincident directions. Figures 9(a) and 9(b) show

the spectra obtained along these high-symmetry directions, respectively. We have centered our attention in occupied states whose binding energy is up to 3 eV below the E_F . In these figures, we have identified different photoemission peaks which are indicated by solid bars. The binding energy of the identified states is plotted versus k_{\parallel} for both symmetry directions in Fig. 9(c) and 9(d). Band structure calculations corresponding to these symmetry directions for $h\nu=32$ eV have been also included in these figures.³³ In the range of binding energy close to the E_F , the band dispersion of the occupied *sp* band is the only noticeable structure. In our ARPES measurements, the *sp* band dispersion in the first BZ appears unresolved for both $[\bar{1}\bar{1}2]$ and $[\bar{2}11]$ directions (Figs. 9(a) and 9(c)). The different states of the *sp* band particularly near the E_F are those defining the FS1, FS2, and FS2' features observed in Fig. 7. In particular, it should be noticed that the shift of the FS2 feature of 0.3 \AA^{-1} at the E_F (Fig. 7) is also observed in the occupied *sp* band up to 3 eV below the E_F .

The two occupied states which are not reproduced by the bulklike Ag band structure are those appearing at normal emission labelled as *QW-sp* and *SS* in Figs. 9(c) and 9(d) with a binding energy of 0.64 and 0.09 eV, respectively. The presence of the *QW-sp* state has been early observed in ARPES measurements in 5-15 ML Ag films onto Si(111)7x7 substrates.⁴² This state has been identified as a film state associated to the confinement of the *sp* band of bulk Ag. The binding energy of confined states depends on film thickness and on the reflection at the interface, in the frame of the phase accumulation model.⁴³ In our 10 ML Ag films, perpendicular confinement of the *sp* states produces confined film-states with a maximum binding energy round to 0.6 eV according with such a thin film thickness. Nevertheless, no trace from confined states with higher quantum number (*n*) than *n*=1 has been detected in our measurements. In any case, this confined state is observed, as expected, to disperse parabolically through the E_F . Out of normal emission, signal from this state tends to vanish due to the loss of coherence. Nevertheless, this state gets close enough to the E_F to produce the ring-like *s*-feature of $\sim 0.26 \text{ \AA}^{-1}$ in radius observed in Fig. 7.

Let us now discuss the behavior of the labelled *SS* state in Figs. 9(c) and 9(d). From band structure calculations in Ag single crystal,⁴⁴ it is not expected the presence of any bulk state at $\bar{\Gamma}$ point of the surface BZ nor some few eV round the E_F . ARPES measurements carried out in Cu(111), Au(111), and Ag(111) single crystal show the presence of a parabolic shallow state round to $\bar{\Gamma}$ point whose dispersion curve is independent on $h\nu$.⁴⁵⁻⁴⁷ This state crosses the E_F at $k_{\parallel}=0.14 \text{ \AA}^{-1}$ from $\bar{\Gamma}$ point in the case of Ag(111).⁴⁸ This state was identified as a Shockley surface state located in the *sp* band gap at the L point of the bulk BZ,⁴⁹ whose existence has been attributed to the break of crystalline periodicity at the surface.⁵⁰ Figures 9(c) and 9(d) also reflect the presence of this surface

state SS crossing the E_F at $k_{\parallel} \sim 0.15 \text{ \AA}^{-1}$. Therefore, the central spot of the s feature observed in Fig. 7 can be attributed to emission at the E_F from this surface state.

The behavior of the h feature observed in Fig. 7 is rather different from that observed for the s features. The cuts of the E_F of the sp band, as shown in Figs. 9(c) and 9(d), appear at the k_{\parallel} -values observed in the FS cut with $h\nu=32$ eV (Fig. 7). Nevertheless, in Figs. 9(a) and 9(b), no trace of any occupied band appears close to the E_F in the spectra measured round to 15° -off normal, corresponding to $k_{\parallel} \sim 0.7 \text{ \AA}^{-1}$. In these spectra, one can only see the trace of a wide tail of the sp band that lies close to the E_F and whose maximum appears 4 eV below it (shadow area in Fig. 9(a)). The presence of the wide tail of the sp band extending just below the E_F has been also observed in Ag(111) and in Cu(100) single crystal by photoemission measurements in normal emission with $h\nu=7-9$ and 21.2 eV and with $h\nu=12-14$ eV, respectively.⁵¹⁻⁵³ This fact has been attributed to indirect transitions induced by the surface. Moreover, this large tail of the sp band is expected mostly to reflect the p -like behavior of deeper sp states. Therefore, the presence of the fluted contour in the 2D FS image of Fig. 7 can be attributed to a consequence of the surface perturbation process involved in the photoemission technique.

C. Two- or three-dimensional behavior of the Fermi surface of the thick Ag(111) films grown on Si substrates

In order to continue the study on the electronic properties of thick Ag films grown onto Si(111)-(7x7) substrates we have centered our further analysis on the 2D or 3D behavior of the FS of these films. This question has been approached in an early work by analyzing the d valence band dispersion of Ag films grown onto Cu(001) single crystal.⁵⁴ In that work, photoemission measurements revealed that the d band shows already a 3D band dispersion for Ag films of 3-5 ML in thickness. The radial extent of d states confines their interactions to nearest neighbors and this interaction is strongly screened by the sp electrons. Nevertheless, The sp states extend to additional neighboring sites. These facts would explain the 3D behavior of the deeper d bands in very thin films, but they would not necessarily imply the same behavior for the FS of such a thin Ag films. Bulklike behavior of the FS has been also observed in 1 ML Ni films on Cu(001).⁵⁵ In this case, the 3D behavior of the sp band has been attributed to the short screening length of electrons in metals and to a strong hybridization between the Ni $sp-d_{z^2}$ hybrid and the Cu sp , both of them crossing the E_F . Through that hybridization, the Bloch periodicity of the substrate is imposed on the electronic wave functions of the film. In Ag films deposited onto semiconducting Si(111)-(7x7) substrates the sp states at the E_F have a strong screening effect inside the substrate. Therefore, the evolution from a 2D to a 3D Ag FS would come from the fulfillment of

periodicity condition of the sp wave functions inside the films.

The different dimensionality of the metallic films can be clearly elucidated by using a tuneable light source. Let us consider the limit case of thin films with 2D electronic properties. In this case, electronic states have a definite k_{\parallel} whereas their k_{\perp} is undefined, since the overlayer has not enough periodicity to ensure crystal momentum conservation in the perpendicular direction. In particular, in the frame of the nearly free-electron model, the FS of 2D Ag(111) metallic films would be expected to be ringlike with the ring axis parallel to the [111] surface vector and contained in the surface BZ. In this case, FS cuts measured with different incident photon energy would show FS features at the same k_{\parallel} values, independently on $h\nu$. Opposite to this, in the case of thin metallic Ag films with 3D electronic properties both k_{\parallel} and k_{\perp} are defined as indicated in Eqs. (1). Therefore, measurements of the cross-sectional cuts of the FS with different $h\nu$ will indicate a clear dependence on k_{\perp} . The analytical relation between the photon energy and the k_{\perp} allow us to scan the bulklike Ag FS (Fig. 4) using different k_{\perp} values, (i.e. by changing the photon energy).

Figures 10(a)- 10(c) show the theoretical 2D cut of the Ag single crystal FS at particular k_{\perp} values probed with $h\nu=32$, 55, and 96 eV, respectively.³³ The $k_{\parallel x}$ and $k_{\parallel y}$ axes correspond to the same symmetry directions that those pointed out in Fig. 5. As expected, all these cuts of the Ag FS put forward the threefold symmetry of the Ag BZ. As increasing $h\nu$, the scanned reciprocal space increases for a given experimental angular range. When the photon energy used was $h\nu=32$ eV, the cut of the Ag FS in the first BZ shows the most relevant features, as described before (Fig. 6(a)). For $h\nu=55$ and 96 eV cross sectional cuts of the Ag FS evidence contours from contiguous BZs. For $h\nu=55$ eV a cross section of the *neck* of the FS at L point could be probed. As it has been discussed in the previous section, thick metallic Ag films deposited onto Si(111)-(7x7) substrates are composed by two domains rotates 60° . Therefore, the FS cuts of these films, with the assumption of a 3D behavior, would show a sixfold symmetry rather than the threefold symmetry of the FS cuts of Ag single crystal for each $h\nu$. Figures 10(d)- 10(f) show the cuts of a 3D FS of Ag films composed of two-domains, calculated at those k_{\perp} values of Figs. 10(a)- 10(c), respectively.

Figures 11(a)- 11(c) show the spectral weight distribution at the E_F measured in a thick Ag film deposited onto Si(111)-(7x7) with $h\nu=32$, 55, and 96 eV, respectively. These images have been plotted in the same conditions that those exposed in Fig. 5. All the FS contours measured at different $h\nu$ exhibit the sixfold symmetry expected for a two-domain Ag film. The FS cut through the first BZ recorded with $h\nu=32$ eV appears as a ringlike structure (FS1 feature in Fig. 7). Using photon energies of $h\nu=55$ and 96 eV, the FS cuts through the first scanned BZ appear as a central bright spot, with a radius of $0.16 \pm 0.08 \text{ \AA}^{-1}$, and a ringlike feature, respectively.

The FS cuts in contiguous BZs also show different features as $h\nu$ increases. No trace from surface states can be distinguished in the $h\nu=55$ and 96 eV images. The fact that the features corresponding to the Ag FS change in k_{\parallel} -plane with increasing $h\nu$ suggests the presence of bulklike electronic states with a clear 3D character.

To perform a quantitative analysis of the measured FS contours, we have calculated the gradient of the spectral weight at the E_F images of Fig. 11, following the procedure suggested by Straub *et al.*⁴⁰ Figures 12(a)- 12(c) show the results of these calculations for $h\nu=32$, 55, and 96 eV, respectively. We have also included the cuts of the bulklike Ag FS calculated for a film composed with 60°-rotated domains (Figs. 10(d)- 10(f)). These plots fairly agree with the experimental results. This good accord between the calculated and the experimental Ag FS contours improves at higher photon energy for all the k_{\parallel} -plane scanned, which suggests that, at high photon energy, the parabolic nearly-free-electron final-state model could be considered as a more realistic approximation. These results definitively put forward the 3D behavior of the FS of 10 ML Ag films deposited onto Si(111)-(7x7) substrates and, in consequence, also point out that parameters defining the FS of these Ag films can be compared to those corresponding to bulklike Ag single crystal.

In order to simultaneously determine k_F and other characteristic parameters of a 3D FS in different symmetry directions, it should be taken into account that the measured k_F values are k_{\perp} -dependent.⁵⁶ Therefore, reliability of the deduced values depends also on a good k_{\perp} determination. In our case, the good concordance obtained in the determination of the Ag FS in the first BZ for all $h\nu$ used in this work suggest that k_{\perp} is reasonably well determined by a constant inner potential $V_o=-11.5$ eV. In any case, the influence of V_o on the determination of a bulklike 3D FS can be overcome with an exhaustive determination of the Ag FS in a well defined range of $h\nu$.

From our results, on one hand we can directly estimate the *neck* radius of the Ag FS at L point from the spectral weight at the E_F image measured with $h\nu=55$ eV, which appears to be $0.16 \pm 0.08 \text{ \AA}^{-1}$. This value of the *neck* radius of the Ag FS is in good agreement with those obtained from other methods.^{57,59,58} On the other side, in the previous section we have estimated the k_F values for different parallel to the surface symmetry directions. As The FS of these films appears to show a 3D behavior, these values of k_F can be also compared with those obtained in Ag single crystal by the Haas-Van Alphen method ($k_F(\Gamma X)=1.258 \text{ \AA}^{-1}$) and those determined by ARPES measurements in quantum-well *sp*-states in Ag(100) films ($k_F(\Gamma X)=1.272 \pm 0.002 \text{ \AA}^{-1}$).^{57,60} In spite of the small discrepancy between these two precedent estimates of k_F , they can be considered comparable since the high-precision of the latter one refers to statistical deviations, without considering the accuracy of the model used.⁶⁰ The fact that our estimate of k_F appears to be slightly lower than the previous ones

can be attributed to the fact that our measurements do not exactly probe the FS cut in the ΓX direction (Fig. 4). A simple geometrical calculation (Fig. 4) will let us to estimate $k_F(\Gamma X)=1.27 \pm 0.06 \text{ \AA}^{-1}$, which is in agreement with those estimates of k_F .

Finally, it should be pointed out that the 3D electronic behavior of the FS of Ag films grown onto Si(111)-(7x7) substrates establishes the workframe in which the determination of the transport properties of such a thick films can be carried out. Our results show that, besides scattering mechanisms involved in electronic transport, electronic states contributing to current can be assumed to be very similar to those characteristic of the bulk metallic material. Therefore, conductivity and transport properties of these films are expected to be mainly determined by impurity, phonon, and defectlike scattering mechanisms of electrons at the E_F with transport parameters close to those of a single crystal material. In fact, conductivity and magnetoconductivity measurements carried out in 10 ML Ag films deposited onto Si(111)-(7x7) substrates at low temperature show a temperature dependence of resistance well described by a Drude model, with a linear coefficient at temperatures higher than 40 K close to that of single crystal.^{28,29} These results appear to contrast with plasmon frequency measurements by energy loss spectroscopy LEED carried out in up to 18 ML Ag films deposited onto Si(111)-(7x7) substrates at different temperatures.⁶¹ In these measurements, plasmon confinement effects into single domains are attributed to lateral extent of grains rather than to a perpendicular confinement in the films, in spite of the metallic conductivity behavior observed in those films. Mean free path of electrons in those films is round to some tens of \AA^{-1} , at low temperature,²⁸ which is of the order of lateral extension of the grains.⁶¹ These facts suggest that strong lateral confinement effects are expected mostly to appear in thinner films, as revealed by magnetoconductivity measurements,²⁹ since they show a higher granular density. In this context, AC conductivity measurements or high-magnetic field conductivity measurements at low temperature rather than DC conductivity measurements in 10 films could be carried out in order to observe lateral confinement effects in 10 ML Ag films. In any case, the fact that films appear to be composed by two 60°-rotated domains may smooth grain boundary scattering mechanisms due to strong hybridization of *sp* states at grain boundaries. This fact would favor that mean free path of electrons is mainly determined by film thickness rather than grain size effects of such a thin films.

IV. SUMMARY AND CONCLUSIONS

Thick Ag films have been deposited onto Si(111)7x7 substrates at room temperature. The electronic properties of these films have been studied by measurements of spectral weight at the E_F at different $h\nu$. With this

technique, cross-sectional cuts of the FS of these films have been obtained for particular values of k_{\perp} . The FS cuts measured in these films reflect clear features with a sixfold symmetry. In order to analyze this result, we have compared the experimental FS cuts with theoretical FS cuts of 3D Ag single crystal. The calculated Ag FS cuts fairly reproduces most of the features observed in the experimental data, but the sixfold symmetry of the Ag films FS is not reproduced. These facts suggest that the loss of symmetry order of these Ag films is due to their structural composition. In fact, the Ag FS calculated for films composed with two domains rotated 60° fairly reproduces the experimental FS cuts of these films in the whole space of the BZ analyzed.

In addition to this, photoemission traces at the E_F not belonging to bulklike Ag FS have been also detected in the FS of these thick Ag films. They have been attributed to the presence of surface states, which are located in the sp band gap at the L point of the BZ, and to sp -quantum states of these films. Also, additional features have been detected coming from the tail of deep sp states.

The fact that the FS contours of thick Ag films are well reproduced by bulklike Ag FS cut for a particular k_{\perp} value encouraged us to determine the dimensionality of the FS of these films. In order to solve this point, FS mapping was carried out by measuring Ag FS cuts with different photon energies. The FS contours measured at $h\nu=32, 55,$ and 96 eV reflect different traces of the FS as $h\nu$ increases, which puts forward the 3D behavior of the FS of these films. The bulklike Ag FS cuts calculated for films composed by two-domains, with k_{\perp} values corresponding to $h\nu=32, 55,$ and 96 eV, fit the FS cuts of these thick Ag films in the whole BZ scanned.

ACKNOWLEDGMENTS

This work was financed by DGICYT (Spain) (Grant No. PB-97-1199) and the Large Scale Facilities program of the EU to LURE. Financial support from the Comunidad Autónoma de Madrid (Project No. 07N/0042/98) is also acknowledged. J.F.S.-R. acknowledges financial support from the Ministerio de Educación y Cultura of Spain.

* Electronic address: asensio@lure.u-psud.fr
and mcasensio@icmm.csic.es

¹ D. Haneman, Rep. Prog. Phys. **50**, 1045 (1987).

² S. Hasegawa, X. Tong, S. Takeda, N. Sato, and T. Nagao, Prog. in Surf. Sci. **60**, 89 (1999).

³ R. Losio, K.N. Altmann, and F.J. Himpsel, Phys. Rev. B **61**, 10845 (2000).

⁴ Y. Fukaya and Y. Shigeta, Phys. Rev. Lett. **85**, 5150 (2000).

⁵ St. Tosch and H. Neddermeyer, Phys. Rev. Lett. **61**, 349 (1988).

⁶ A. Shibata, Y. Kimura, and K. Takayanagi, Surf. Sci. **303**, 161 (1994).

⁷ H. Hirayama, H. Okamoto, and K. Takayanagi, Phys. Rev. B **60**, 14260 (1999).

⁸ K.J. Wan, X.F. Lin, and J. Nogami, Phys. Rev. B **47**, 13700 (1993).

⁹ Z.H. Zhang, S. Hasegawa, and S. Ino, Phys. Rev. B **55**, 9983 (1997).

¹⁰ K. Sumitomo, K. Tanaka, Y. Izawa, I. Katayama, F. Shoji, K. Oura, and T. Hanawa, Appl. Surf. Sci. **41-42**, 112 (1989).

¹¹ Y. Gotoh, S. Ino, and H. Komatsu, J. Crystal Growth **56**, 498 (1982).

¹² Y. Gotoh and S. Ino, Thin Solid Films **109**, 255 (1983).

¹³ J.E. Rowe and H. Ibach, Phys. Rev. Lett. **32**, 421 (1974).

¹⁴ G.V. Hansson, R.I.G. Uhrberg, and S.A. Flodström, J. Vac. Sci. Technol. **16**, 1287 (1979).

¹⁵ F. Houzay, G.M. Guichar, R. Pinchaux, P. Thiry, Y. Petroff, and D. Dagneaux, Surf. Sci. **99**, 28 (1980).

¹⁶ F.J. Himpsel, D.E. Eastman, P. Heimann, B. Reihl, C.W. White and D.M. Zehner, Phys. Rev. B **24**, 1120 (1981).

¹⁷ R.I.G. Uhrberg, G.V. Hansson, J.M. Nicholls, P.E.S. Persson, and S.A. Flodström, Phys. Rev. B **31**, 3805 (1985).

¹⁸ R.I.G. Uhrberg, T. Kaurila, and Y.-C. Chao, Phys. Rev. B **58**, R1730 (1998).

¹⁹ R.J. Hamers, R.M. Tromp, and J.E. Demuth, Phys. Rev. Lett. **56**, 1972 (1986).

²⁰ R. Wolkow and Ph. Avouris, Phys. Rev. Lett. **60**, 1049 (1988).

²¹ F.J. Himpsel, G. Hollinger, and R.A. Pollak, Phys. Rev. B **28**, 7014 (1983).

²² R. Schad, S. Heun, T. Heidenblut, and M. Henzler, Phys. Rev. B **45**, 11430 (1992).

²³ D. Fick, R. Veith, H.D. Ebinger, H.J. Jänsch, C. Weindel, H. Winnefeld, and J.J. Paggel, Phys. Rev. B **60**, 8783 (1999).

²⁴ A. Samsavar, T. Miller, and T.-C. Chiang, Phys. Rev. B **42**, 9245 (1990).

²⁵ M. Henzler, *Surface Physics of Materials I*, Ed. J.M. Blakely, Academic Press (New York 1975) p. 241.

²⁶ Y. Hasegawa, I.-W. Lyo, and P. Avouris, Surf. Sci. **357-358**, 32 (1996).

²⁷ S. Heike, S. Watanabe, Y. Wada, and T. Hashizume, Phys. Rev. Lett. **81**, 890 (1998).

²⁸ M. Henzler, T. Lüer, and A. Burdach, Phys. Rev. B **58**, 10046 (1998).

²⁹ M. Henzler, T. Lüer, and J. Heitmann, Phys. Rev. B **59**, 2383 (1999).

³⁰ J. Avila, C. Casado, M.C. Asensio, J.L. Pérez, M.C Muñoz, And F. Soria, J. Vac. Sci. Technol. A **13**, 1501 (1995).

³¹ A. Mascaraque, J. Avila, C. Teodorescu, M.C. Asensio, and E.G. Michel, Phys. Rev. B **55**, R7315 (1997).

³² N.W. Ashcroft and N.D. Mermin, *Solid State Physics*, Saunders College, Philadelphia, PA.

³³ D.A. Papaconstantopoulos, *Handbook of the Band Structure of Elemental Solids* (Plenum, New York, 1986). The

- band diagrams have been calculated with an empirical second-neighbor tight-binding Hamiltonian. The orthogonal two-center tight-binding parameters given by Papaconstantopoulos have been used.
- ³⁴ S.C. Wu, H. Li, J. Sokolov, J. Quinn, Y.S. Li, and F. Jona, *J. Phys.: Condens. Matter.* **1**, 7471 (1989).
- ³⁵ S. Hüfner, *Photoelectron Spectroscopy*, Springer Series in Solid-State Sciences n. 82 (Springer-Verlag, Berlin Heidelberg, 1995).
- ³⁶ J. Mesot, A. Kaminski, H.M. Fretwell, M. Randeria, J. C. Campuzano, H. Ding, M. R. Norman, T. Takeuchi, T. Sato, T. Yokoya, T. Takahashi, I. Chong, T. Terashima, M. Takano, T. Mochiku, and K. Kadowaki, *cond-mat/9910430*.
- ³⁷ P. Aebi, J. Osterwalder, P. Schwaller, L. Schlapbach, M. Shimoda, T. Mochiku, and K. Kadowaki, *Phys. Rev. Lett.* **72**, 2757 (1994).
- ³⁸ M. Lindroos, and A. Bansil, *Phys. Rev. Lett.* **77**, 2985 (1996).
- ³⁹ V. Pérez-Dieste J.F. Sánchez-Royo, J. Avila, and M.C. Asensio, *unpublished*.
- ⁴⁰ Th. Straub, R. Claessen, P. Steiner, S. Hüfner, V. Eyert, K. Friemelt, and E. Bucher, *Phys. Rev. B* **55**, 13473 (1997).
- ⁴¹ V.N. Strocov, R. Claessen, G. Nicolay, S. Hüfner, A. Kimura, A. Harasawa, S. Shin, A. Kakizaki, P.O. Nilsson, H.I. Starnberg, and P. Blaha, *Phys. Rev. Lett.* **81**, 4943 (1998).
- ⁴² A. L. Wachs, A.P. Shapiro, T.C. Hsieh, and T.-C. Chiang, *Phys. Rev. B* **33**, 1460 (1986).
- ⁴³ N.V. Smith, N.B. Brookes, Y. Chang, and P.D. Johnson, *Phys. Rev. B* **49**, 332 (1994).
- ⁴⁴ H. Eckardt, L. Fritsche, and J. Noffke, *J. Phys. F* **14**, 97 (1984).
- ⁴⁵ P. Heimann, H. Neddermeyer, and H.F. Roloff, *J. Phys. C* **10**, L17 (1977).
- ⁴⁶ S.D. Kevan, *Phys. Rev. B* **33**, 4364 (1986).
- ⁴⁷ F. Reinert, G. Nicolay, S. Schmidt, D. Ehm, and S. Hüfner, *Phys. Rev. B* **63**, 115415 (2001).
- ⁴⁸ B.A. McDougall, T. Balasubramanian, E. Jensen, *Phys. Rev. B* **51**, 13891 (1995).
- ⁴⁹ J.G. Nelson, S. Kim, W.J. Gignac, R. S. Williams, J.G. Tobin, S.W. Robey, and D.A. Shirley, *Phys. Rev. B* **32**, 3465 (1985).
- ⁵⁰ P.M. Echenique and J.B. Pendry, *J. Phys. C* **11**, 2065 (1978).
- ⁵¹ T. Miller, W.E. McMahon, and T.-C. Chiang, *Phys. Rev. Lett.* **77**, 1167 (1996).
- ⁵² T. Michalke, A. Gerlach, K. Berge, R. Matzdorf, and A. Goldmann, *Phys. Rev. B* **62**, 10544 (2000).
- ⁵³ E.D. Hansen, T. Miller, and T.-C. Chiang, *Phys. Rev. Lett.* **78**, 2807 (1997).
- ⁵⁴ J.G. Tobin, S.W. Robey, L.E. Klebanoff, and D.A. Shirley, *Phys. Rev. B* **28**, 6169 (1983).
- ⁵⁵ G.J. Mankey, K. Subramanian, R.L. Stockbauer, and R.L. Kurtz, *Phys. Rev. Lett.* **78**, 1146 (1997).
- ⁵⁶ P. Aebi, J. Osterwalder, R. Fasel, D. Naumović, and L. Schlapbach, *Surf. Sci.* **307-309**, 917 (1994).
- ⁵⁷ P.T. Coleridge and I.M. Templeton, *Phys. Rev. B* **25**, 7818 (1982).
- ⁵⁸ A.H. McDonald, J.M. Daams, S.H. Vosko, and D.D. Koelling, *Phys. Rev. B* **25**, 713 (1982).
- ⁵⁹ G. Fuster, J.M. Tyler, N.E. Brener, J. Callaway, and D. Bagayoko, *Phys. Rev. B* **42**, 7322 (1990).
- ⁶⁰ J.J. Pagel, T. Miller, and T.-C. Chiang, *Phys. Rev. B* **61**, 1804 (2000).
- ⁶¹ F. Moresco, M. Rocca, T. Hildebrandt, and M. Henzler, *Phys. Rev. Lett.* **83**, 2238 (1999).

FIG. 1. Bulk Brillouin zone of the fcc Ag single crystal. Its projection on the (111)-plane, that is the surface Brillouin zone, is also drawn. The main points and high-symmetry directions of both the bulk and the surface Brillouin zones are also indicated.

FIG. 2. Fermi surface of bulk Ag. To clarify the illustration the bulk Ag Brillouin zone is also drawn, together with its main points and high symmetry directions.

FIG. 3. Bulk Ag band structure calculated by using a tight-binding method for $h\nu=32$ eV in: (a) the $[\bar{1}10]$ and (b) in the $[\bar{1}\bar{1}2]$ and $[\bar{2}11]$ high-symmetry directions. The binding energy of the bands is referred to the E_F , whose position is indicated in dotted lines. States lying at the E_F are labelled from E1 to E5. (c) Corresponding Ag FS cut represented in the k_{\parallel} -plane. Points of the FS cut labelled as E1-E5 correspond to states lying at the E_F indicated in (a) and (b).

FIG. 4. Intersection of final-state nearly free electron parabolas for $h\nu=32$, 55, and 96 eV with the typical polygons of the Ag Brillouin zone in two selected directions. The so-called dog-bones structures of the FS cross-section in the selected plane are also shown. Notice that, by changing $h\nu$, the whole three-dimensional Brillouin zone can be studied.

FIG. 5. (color) Spectral weight at the E_F in a region of the k_{\parallel} -plane measured in a thick Ag film deposited onto Si(111)7x7 with $h\nu=32$ eV.

FIG. 6. (a) Fermi surface cut of Ag single crystal represented in the k_{\parallel} -plane as calculated by using a tight-binding method for $h\nu=32$ eV. The different features obtained are labelled as FS1, FS2, and FS2'. The Fermi vector is also indicated. The corresponding Ag surface Brillouin zone is plotted at the bottom of this figure, in which symmetry directions of the parallel wave vector are indicated. (b) The same that (a) calculated for a situation of a film composed with two 60° -rotated domains. At the bottom of this figure, it is illustrated the fact that the surface Brillouin zones of both domains appear to be overlapped in ARPES.

FIG. 7. (color) Gradient of the spectral weight at the E_F shown in Fig. 5. The Fermi surface cut calculated for $h\nu=32$ eV in the case of a Ag film with 60° -rotated domains is also plotted in dotted lines. The different features observed and the Fermi vector are indicated. The misfit in the position of the FS2 feature is also indicated (ΔFS2).

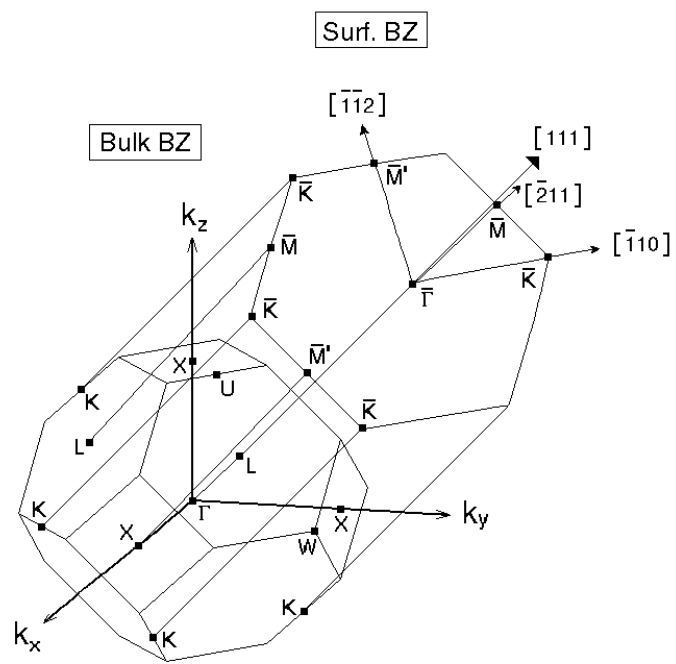
FIG. 8. Spectral weight at the E_F measured in: (a) the $\langle\bar{1}10\rangle$ and (b) the $\langle\bar{1}\bar{1}2\rangle$ and $\langle\bar{2}11\rangle$ overlapped directions (solid curves). The gradient of each profile is also plotted under the corresponding one as dotted curves. The value of k_F extracted from these gradients is drawn, as average value. Its position is marked by a solid vertical bar.

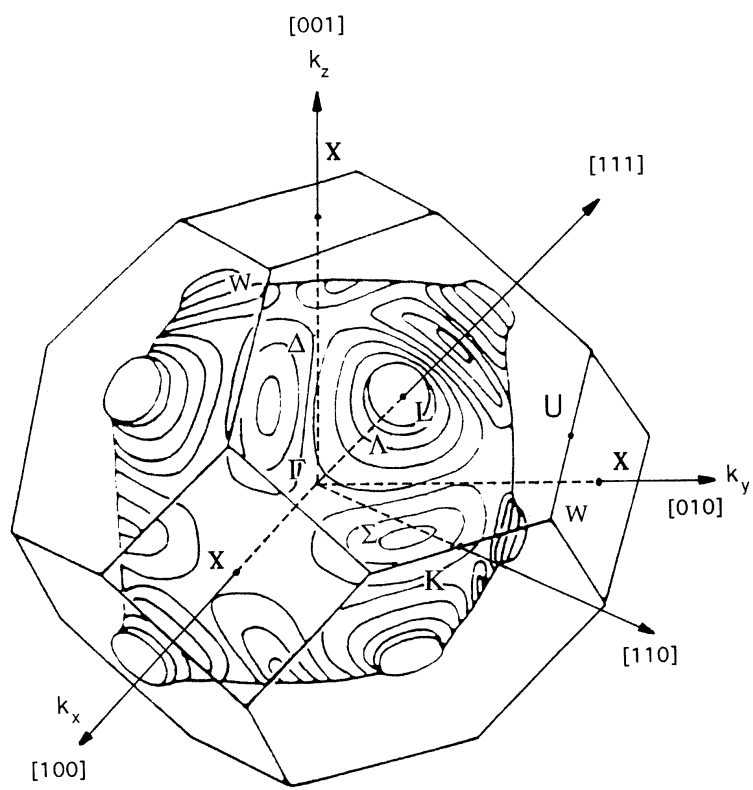
FIG. 9. Energy distribution curves measured in a thick Ag film with $h\nu=32$ eV along: (a) the overlapped $[\bar{1}\bar{1}2]$ and $[\bar{2}11]$ and (b) the $[\bar{1}10]$ symmetry directions. The binding energy of these curves is referred to the E_F . The value of Θ_{off} is given for some of the curves, being the rest of them equally Θ_{off} -separated between two consecutive labelled ones. The different peaks identified have been marked by small solid bars. A dashed area in the $\Theta_{off}=14^\circ$ curve has been labelled as *sp-tail*. (c) and (d) (circles, full circles, triangles) Band dispersion diagram extracted from the peaks identified in (a) and (b), respectively. (crosses, plus, diamonds) Band dispersion calculated with $h\nu=32$ eV along the $[\bar{1}\bar{1}2]$, $[\bar{2}11]$, and $[\bar{1}10]$ symmetry directions, respectively. The E_F position is marked by dotted lines. Bulk states of the calculated bands lying at the E_F are labelled as in Fig. 6(a).

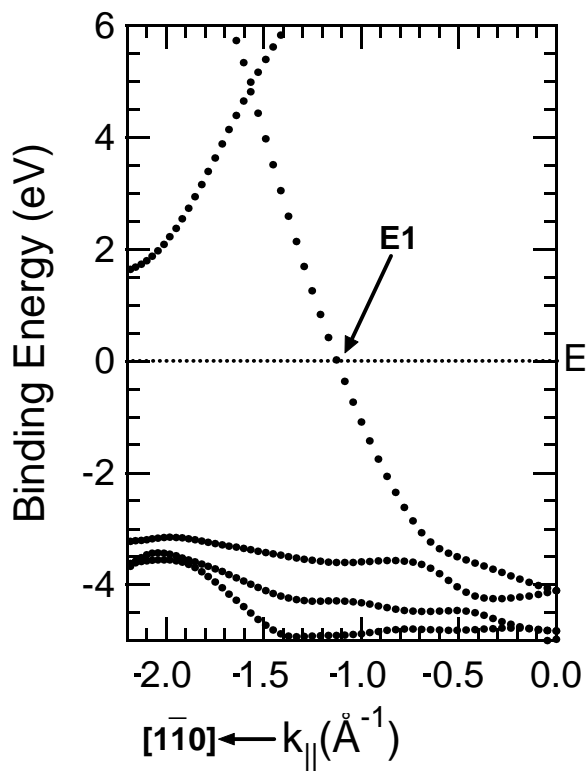
FIG. 10. On the left side, Fermi surface cuts in the k_{\parallel} -plane of Ag(111) single crystal as calculated by a tight-binding method for $h\nu=32, 55,$ and 96 eV. On the right side, These Fermi surface cuts calculated for a situation of Ag films composed by two 60° -rotated Ag domains.

FIG. 11. (color) (a)-(c) Spectral weight at the E_F in a region of the k_{\parallel} -plane measured in a thick Ag film deposited onto Si(111)-(7x7) with $h\nu=32, 55,$ and 96 eV, respectively.

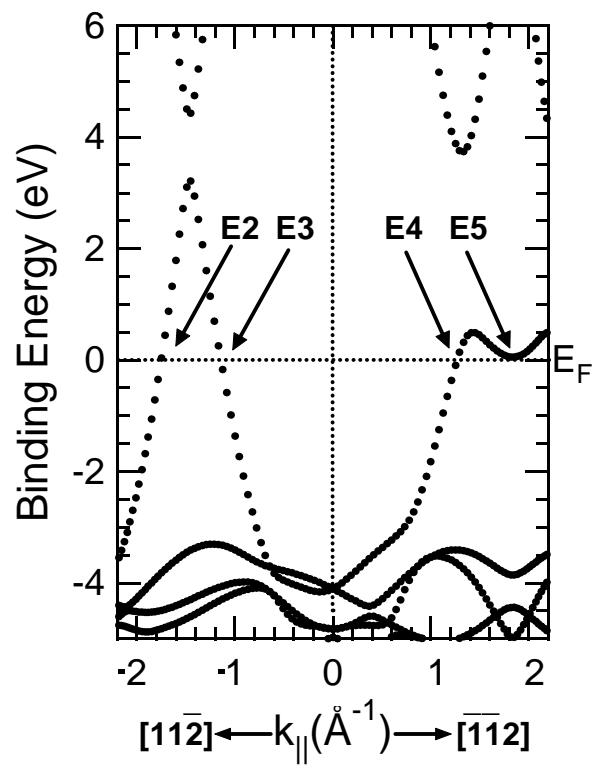
FIG. 12. (color) (a)-(c) Gradient of the spectral weight images at the E_F shown in Fig. 11, which were obtained with $h\nu=32, 55,$ and 96 eV, respectively. The corresponding calculated Fermi surface cuts in the case of a Ag film with two 60° -rotated domains are also plotted in dotted lines.



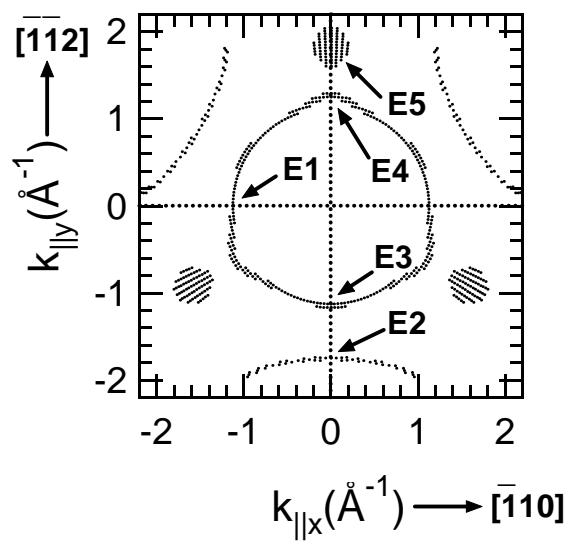




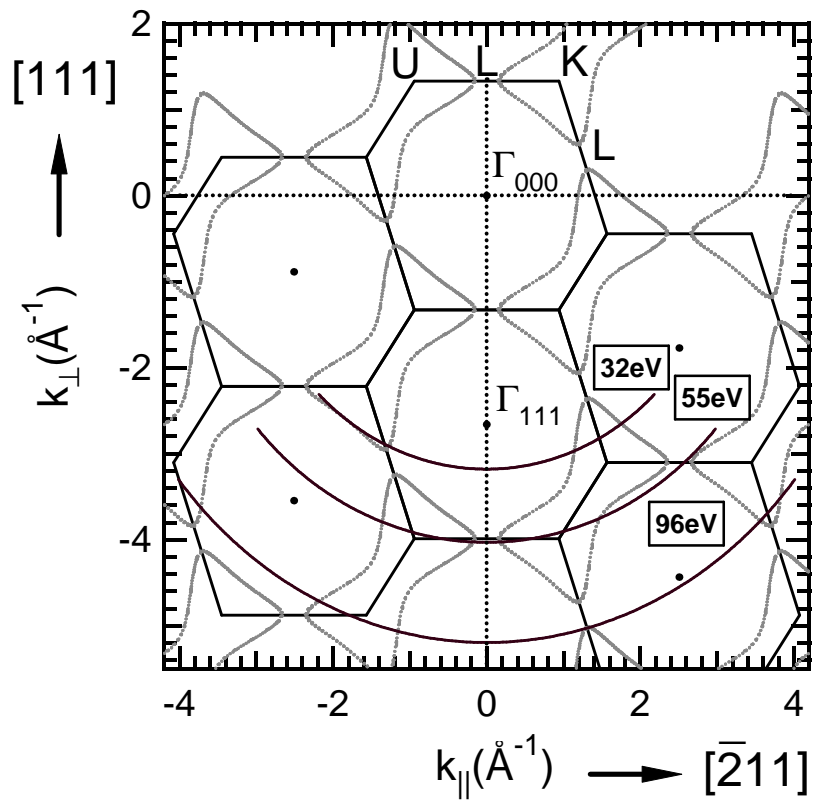
(a)



(b)



(c)

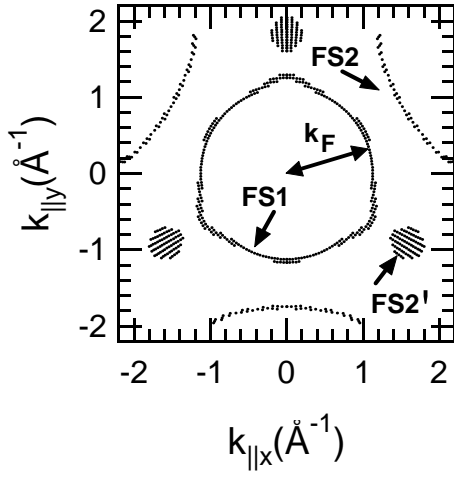


This figure "fig5.jpg" is available in "jpg" format from:

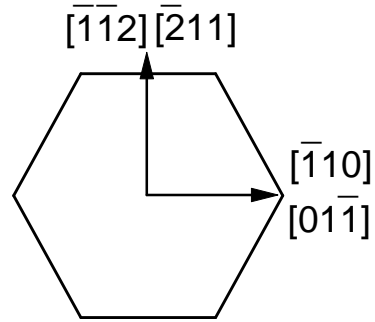
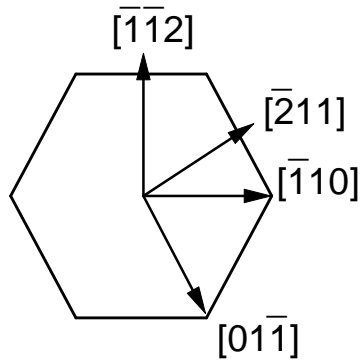
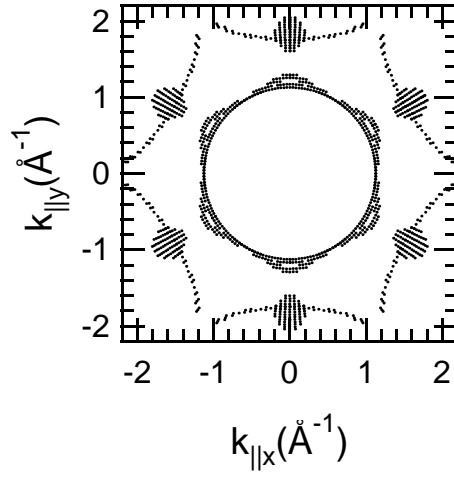
<http://arxiv.org/ps/cond-mat/0104186v1>

$h\nu=32$ eV

(a)

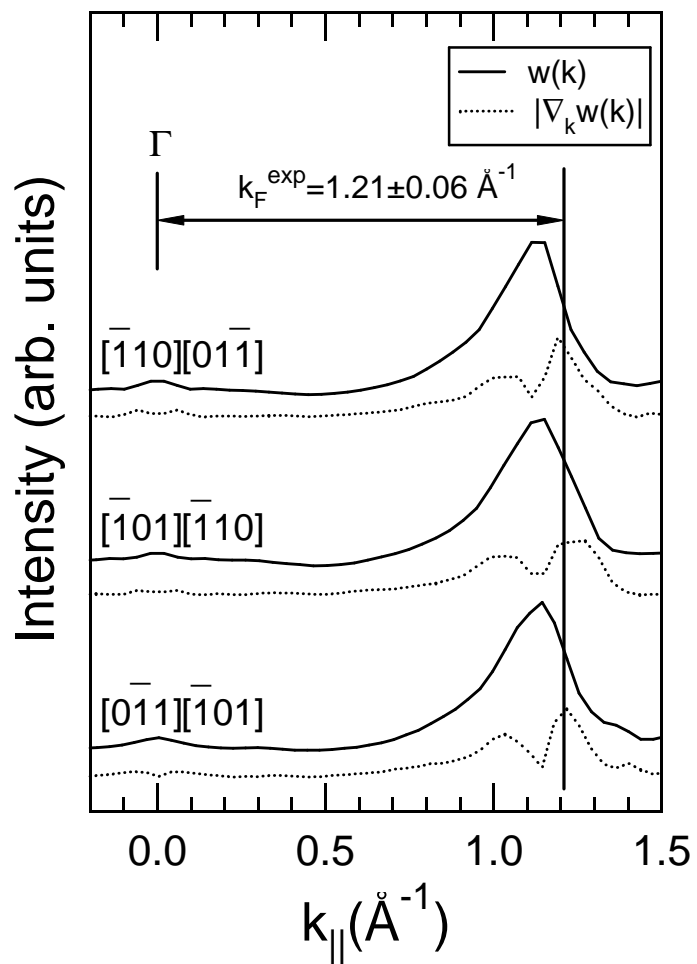


(b)

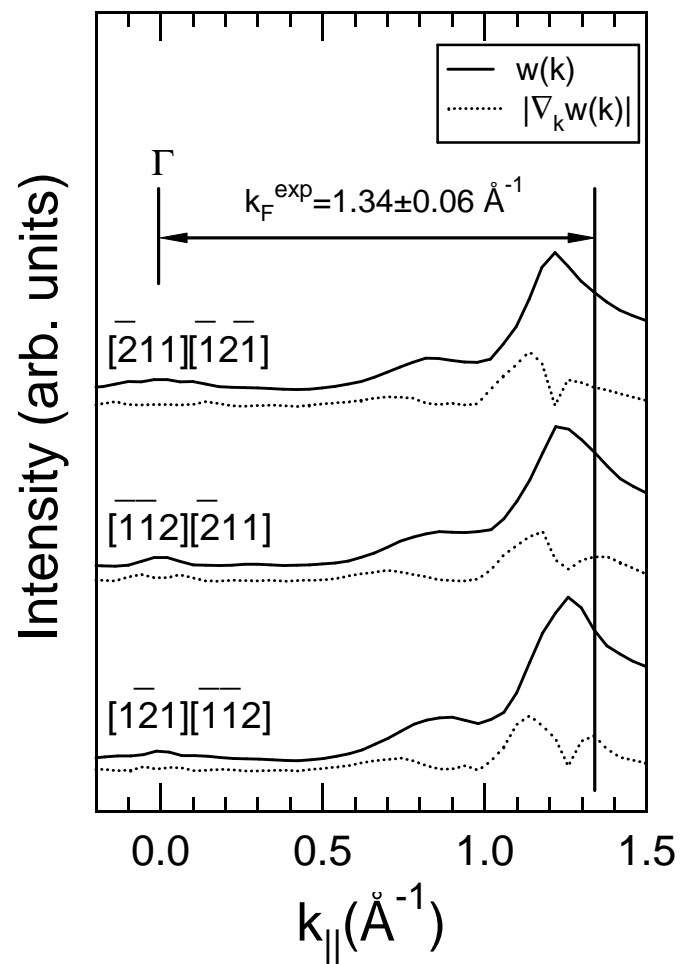


This figure "fig7.jpg" is available in "jpg" format from:

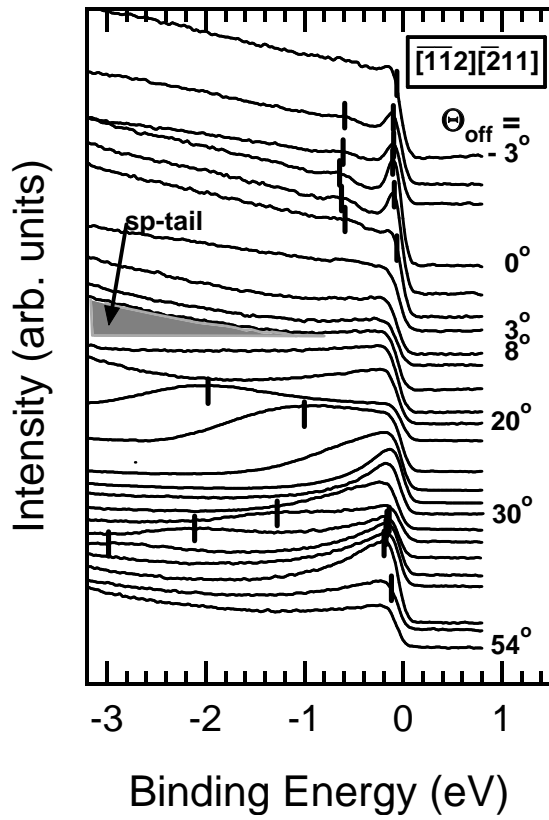
<http://arxiv.org/ps/cond-mat/0104186v1>



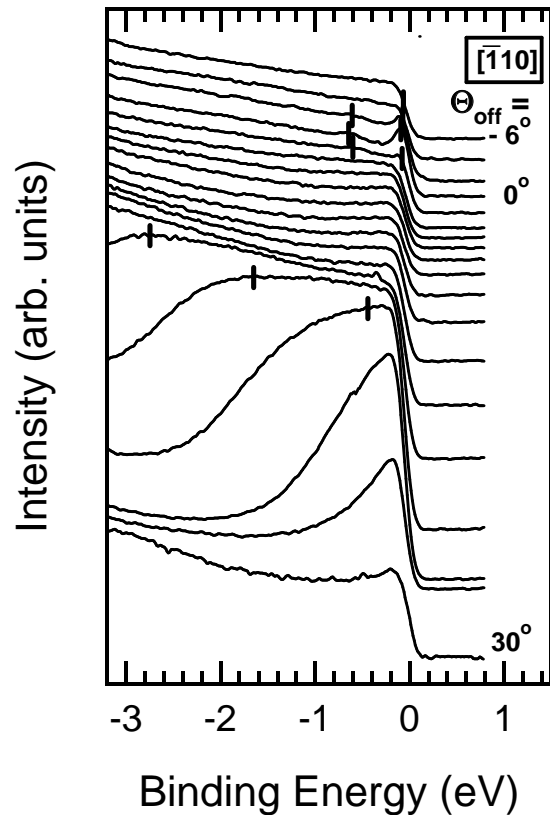
(a)



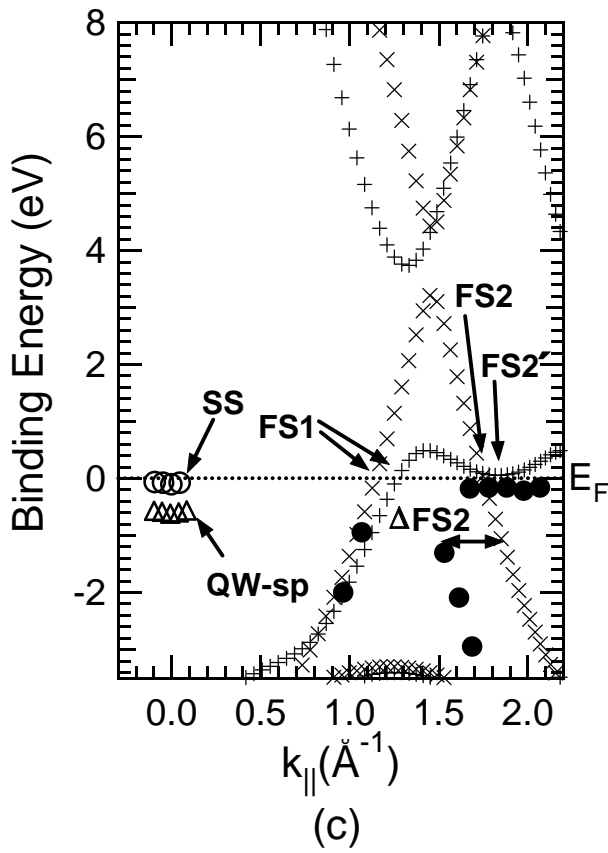
(b)



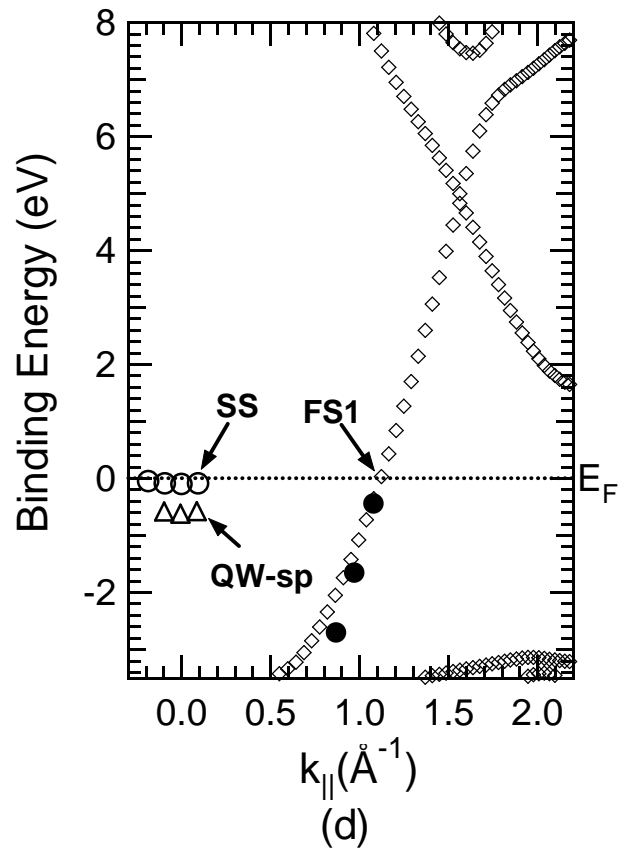
(a)



(b)

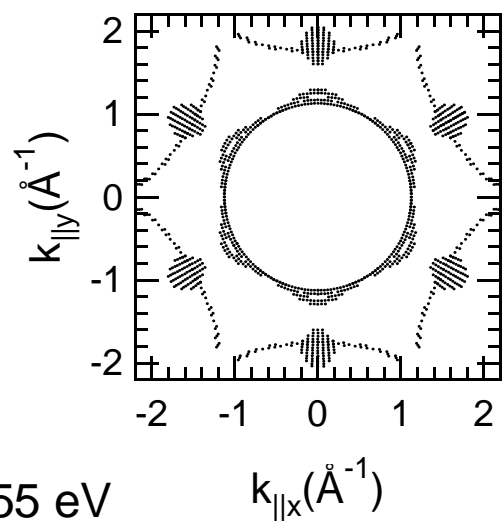
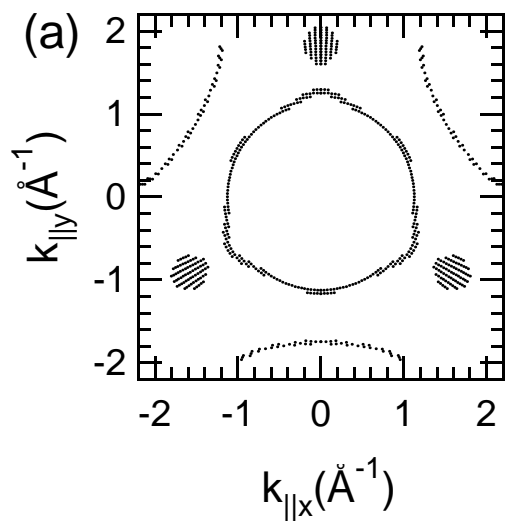


(c)

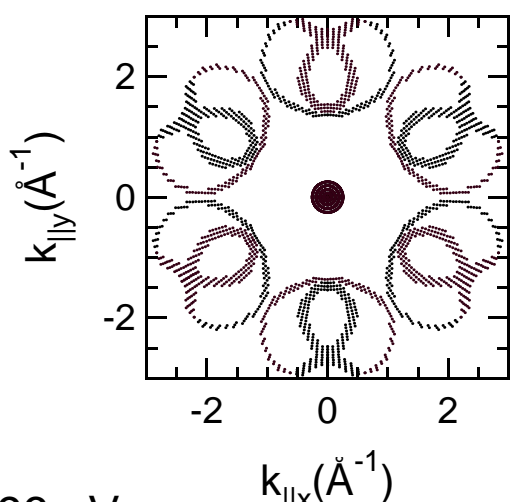
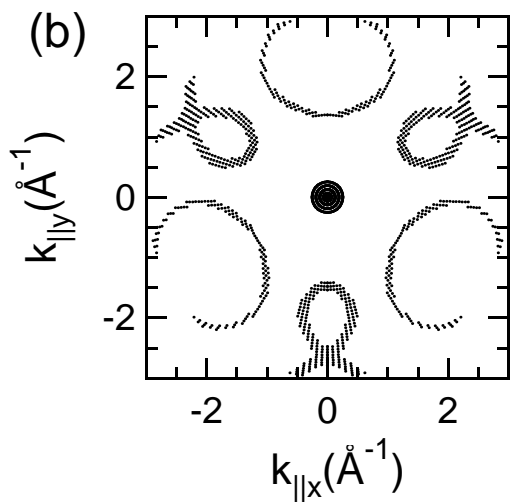


(d)

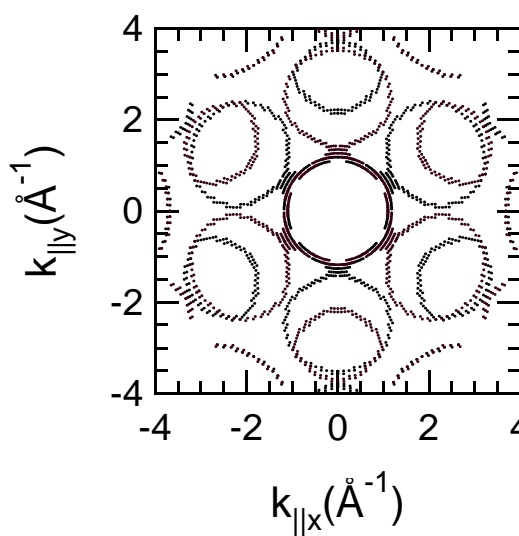
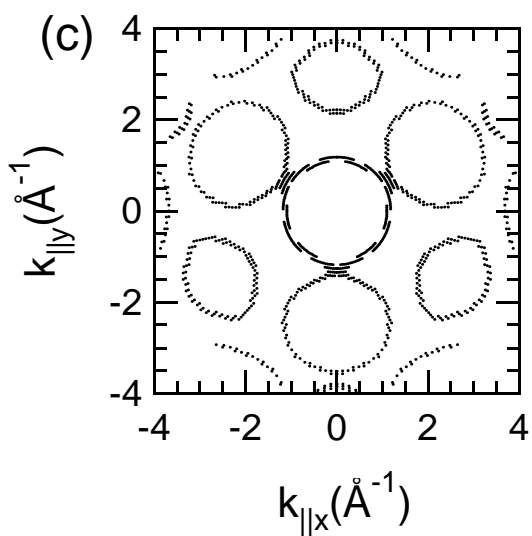
$h\nu=32$ eV



$h\nu=55$ eV



$h\nu=96$ eV



This figure "fig11.jpg" is available in "jpg" format from:

<http://arxiv.org/ps/cond-mat/0104186v1>

This figure "fig12.jpg" is available in "jpg" format from:

<http://arxiv.org/ps/cond-mat/0104186v1>